Journal of Solid State Chemistry 206 (2013) 192–198

Contents lists available at ScienceDirect

Journal of Solid State Chemistry

journal homepage: www.elsevier.com/locate/jssc

Crystallinity and compositional changes in carbonated apatites: Evidence from ^{31}P solid-state NMR, Raman, and AFM analysis

John-David P. McElderry [a], Peizhi Zhu [a], Kamal H. Mroue [a,b], Jiadi Xu [b], Barbara Pavan [d], Ming Fang [a], Guisheng Zhao [c], Erin McNerny [c], David H. Kohn [c], Renny T. Franceschi [c], Mark M.Banaszak Holl [a], Mary M.J. Tecklenburg [d,*], Ayyalusamy Ramamoorthy [a,b], Michael D. Morris [a]

[a] Department of Chemistry, University of Michigan, Ann Arbor, MI 48109-1055, USA
[b] Department of Biophysics, University of Michigan, Ann Arbor, MI 48109-1055, USA
[c] School of Dentistry, University of Michigan, Ann Arbor, MI 48109-1055, USA
[d] Department of Chemistry and Science of Advanced Materials Program, Central Michigan University, Mt. Pleasant, MI 48859, USA

ARTICLE INFO

Article history:
Received 30 May 2013
Received in revised form
7 August 2013
Accepted 11 August 2013
Available online 21 August 2013

Keywords:
Crystallinity
Carbonated apatite
MAS NMR
Raman spectroscopy
Bone mineral

ABSTRACT

Solid-state (magic-angle spinning) NMR spectroscopy is a useful tool for obtaining structural information on bone organic and mineral components and synthetic model minerals at the atomic-level. Raman and ^{31}P NMR spectral parameters were investigated in a series of synthetic B-type carbonated apatites (CAps). Inverse ^{31}P NMR linewidth and inverse Raman PO_4^{3-} ν_1 bandwidth were both correlated with powder XRD *c-axis* crystallinity over the 0.3–10.3 wt% CO_3^{2-} range investigated. Comparison with bone powder crystallinities showed agreement with values predicted by NMR and Raman calibration curves. Carbonate content was divided into two domains by the ^{31}P NMR chemical shift frequency and the Raman phosphate ν_1 band position. These parameters remain stable except for an abrupt transition at 6.5 wt% carbonate, a composition which corresponds to an average of one carbonate per unit cell. This near-binary distribution of spectroscopic properties was also found in AFM-measured particle sizes and Ca/P molar ratios by elemental analysis. We propose that this transition differentiates between two charge-balancing ion-loss mechanisms as measured by Ca/P ratios. These results define a criterion for spectroscopic characterization of B-type carbonate substitution in apatitic minerals.

1. Introduction

Crystallinity is generally regarded as one of several metrics that are used to define optimum bone material properties. Shifting of bone mean crystallinity and increasing crystallinity variability over time have been associated with bone fragility [1,2]. Bone mineral crystallinity generally increases with age [3,4]; and higher crystallinity is characteristic of osteoporotic bone [5–7].

Bone is a dual-phase material composed of an organic matrix reinforced with a rigid mineral. The main component of the organic phase is type I collagen (~90%), along with small amounts of heterotypic collagens and various non-collagenous proteins and polysaccharides [8,9]. Bone mineral, on the other hand, has a structure similar to the mineral calcium hydroxyapatite, $Ca_{10}(PO_4)_6(OH)_2$. However, unlike calcium hydroxyapatite, bone mineral is poorly crystalline and nonstoichiometric. In addition to very small amounts of other ions (such as Na^+, Mg^{2+}, F^-), bone mineral contains 5–8 wt% CO_3^{2-}. Predominantly, the carbonate is present as B-type carbonate, i.e. with carbonate substituting for phosphate ions [10,11].

Synthetic B-type carbonated apatites (CAps) are commonly used as model compounds for investigating chemical properties of bone mineral, and have been the subject of extensive research due to their importance in a variety of biomedical applications such as grafts and scaffolds for reconstructing or regenerating bone defects, osteoconductive implant coatings, and vehicles for drug delivery [12,13]. Several research groups have synthesized bone-like apatites under near-physiological conditions [14,15]. The biological response to synthetic apatites, both in vitro and in vivo, depends, in part, on the degree of carbonation and crystallinity of the apatite.

In X-ray diffraction (XRD) crystallography, apatite crystallinity is conventionally defined by the Debye–Scherrer equation, where average size of the crystalline domains along a crystallographic dimension is inversely proportional to the full-width at half-maximum (FWHM) of a reflection band along that axis. *c-axis* crystallinities were used for apatite sizing throughout this study

* Corresponding author. Fax: +1 989 774 3883.
E-mail address: mary.tecklenburg@cmich.edu (M.M.J. Tecklenburg).

0022-4596/$ - see front matter © 2013 Elsevier Inc. All rights reserved.
http://dx.doi.org/10.1016/j.jssc.2013.08.011

because crystallites in bone are elongated mostly along the *c*-axis [16,17]. Lattice strain also contributes to reflection band broadening, which can have a contribution in imperfect crystallites. Although crystal length measures can be separated from lattice strain as part of a Rietveld refinement, such analyses can introduce a considerable amount of error and are not often used in studies of nonstoichiometric minerals and bone, where crystallinity is typically low [3,18,19].

Similar crystallinity/inverse bandwidth relationships are also used in spectroscopic techniques for mineral analysis. Fourier transform infrared spectroscopy (FTIR) has long been used for measuring mineral crystallinity in bone and apatite [7,20]. While FTIR bandwidths are sensitive to crystallinity, band area ratios also indicate crystallinity and are the preferred metric for most bone applications [7,20–22]. Akkus and co-workers have correlated CAp crystallinity and inverse Raman bandwidths, and have applied these correlations to bone mineral [23–25]. Similar Raman/crystallinity correlations have been reported by Kazanci et al. [26] and Turunen et al. [27]. Linear correlations with powder diffraction data rather than calculations from a governing equation are usually used to define crystallinity in these techniques.

Solid-state NMR spectroscopy is a powerful tool to obtain high-resolution structural information on apatite and bone mineral at the atomic-level [28–33]. ^{31}P and ^{43}Ca magic-angle spinning (MAS) NMR experiments have been used to study structural changes in apatite and bone mineral [34–40]. Over the past decade, solid-state NMR methodologies have also been used to study the crystallinity of semi-crystalline polymers [41–43]. To the best of our knowledge, no analogous correlations have been reported for solid-state nuclear magnetic resonance (NMR) data on CAps or bone, although broader NMR line shapes have been observed in disordered minerals [38,44,45].

In this study, we hypothesized that apatite crystallinity measures are obtainable from ^{31}P NMR spectra and that an inverse linewidth relationship exists, similar to Raman spectra of bone mineral. We undertook a systematic study, by NMR and Raman spectroscopy, of the crystallinity of synthetic carbonated apatites and we investigated the applicability of the same measures to two examples of bone mineral from bovine femur and murine femur. The bone samples are representative of the typical carbonate levels in bone mineral while the synthetic CAps span a much broader range of carbonate substitution than naturally occurs in bone. The results from ^{31}P MAS NMR measurements on the series of B-type CAps with various carbonate levels were analyzed and compared with crystallinity measurements performed by powder X-ray diffraction (XRD) and Raman spectroscopy. ^{31}P NMR isotropic chemical shifts and their linewidths (FWHM) were extracted from the experimentally measured line shapes, and related to percent carbonation. Bovine and murine bone powders were also studied by these spectroscopies and compared to the CAps. While crystallinity by XRD provides information about the crystal domain size, we supplemented our measurements with atomic force microscopy (AFM) as a direct measure of total particle size irrespective of axis orientation. AFM has been used as a direct measure of bone mineral nanoparticles, and more recently, periodicity of bone matrix spacings [18,46,47].

In addition, we explored the nature of carbonate composition dependence on apatite crystallinity. We observed that NMR and Raman spectroscopy show similar carbonate composition-dependent variation in the position of ^{31}P isotropic chemical shift and the wavenumber of the PO_4^{3-} ν_1 symmetric stretch. The composition dependence is nearly binary and remarkably consistent across analysis techniques; however, this dependence was not observed in the crystallinity metrics associated with NMR linewidths and Raman bandwidths. We propose that different mechanisms of charge balancing ion-loss (ion vacancies) account for the differences in spectral frequency between low and high levels of carbonate substitution in apatitic minerals. We anticipate that our results will contribute to an improved understanding of ion substitution in synthetic and natural apatitic minerals and will broaden the capabilities of solid state NMR in that pursuit.

2. Materials and methods

2.1. Sample preparation

Our study includes a series of synthetic carbonated apatites (CAps) in addition to bovine femoral bone (BF) powder taken from the mid-diaphyseal cortex and powder from six-month old murine whole femora (MF). The CAp series was synthesized at low temperatures (80–90 °C) following the aqueous precipitation method published by Penel et al. for B-type apatites [48]. Variations in the published method were limited to replacing sodium phosphate and sodium carbonate with the corresponding ammonium salts for the purpose of reducing cationic substitution into Ca(I) and Ca(II) sites.

Composition of the synthetic CAp samples was determined by ICP-OES for calcium and phosphorus content using a Perkin Elmer Optima 3000. Emission lines used were 317.9333 nm for Ca and 213.617 nm for P (under N_2 purge). The samples were dissolved in 2% wt/vol nitric acid in ultrapure water (resistivity 17–18 Mohm cm, <0.03 ppm dissolved solids). Standard calcium and phosphorus solutions from Perkin Elmer were used for calibration and a standard hydroxyapatite sample from the National Institute for Standards and Technology (NIST; SRM 2910) was used as a check standard.

FTIR spectra for carbonate analysis were acquired using a Nicolet Magma FTIR spectrometer (Thermo Electron Corp., Madison, WI) with a KBr beamsplitter and DTGS detector on KBr pellets. At a resolution of 4 cm^{-1}, 250 scans were ratioed against an air background and the spectra were processed to obtain baselines and peak heights in absorbance units using Omnic software (Thermo Electron Corp.).

The carbonate content of ten apatite samples, with carbonate levels that varied from 0.2 to 10.3 wt%, was determined by coulometric titration after heating and collecting CO_2 gas in an absorption cell containing lithium hydroxide (Galbraith Laboratories, Knoxville, TN). A calibration curve based on the absorbance ratio of FTIR peaks at 1454 cm^{-1} (carbonate) to 565 cm^{-1} (phosphate) versus wt% carbonate (by chemical analysis) was used to determine the carbonate content of the CAp samples used in this study.

Bovine femora were harvested from freshly slaughtered animals (2–4 years old). Femora were stripped of soft tissue, and cortical bone specimens were prepared from central diaphyseal sections. Each diaphysis was sectioned on a band saw into parallelepipeds. Calcium-buffered saline was used during all machining steps to avoid heating the bone and to maintain tissue saturation and ionic balance. Sections randomly chosen from an inventory of ten femora with respect to longitudinal and circumferential location were milled into a powder while cryogenically cooled with liquid nitrogen. Right and left femora were collected from two mice, (male, C57BL.6, age 6 months), and milled into a powder in a similar fashion to the bovine bone powder. Carbonate content for these biological specimens was determined by comparing the Raman carbonate-to-phosphate ratio of the 1070 cm^{-1} (carbonate) and $\sim$960 cm^{-1} (phosphate) bands, as described in Ref. [49], to a calibration curve consisting of carbonate-to-phosphate values measured from the CAp series.

2.2. Nuclear magnetic resonance experiments

All solid-state ^{31}P NMR experiments were carried out on a Varian/Agilent VNMRJ 600 MHz NMR spectrometer (operating at a Larmor frequency of 242.8 MHz for ^{31}P) equipped with a 4-mm

triple-resonance magic-angle spinning (MAS) probe at room temperature (25 °C) under 10 kHz MAS conditions. The ^{31}P NMR spectra were recorded using a single 5 μs excitation pulse, a 20 s recycle delay, and a 80 kHz proton decoupling during signal acquisition using the SPINAL-64 pulse scheme [50]. Phosphorus-31 NMR chemical shifts were referenced with respect to 85% aqueous phosphoric acid. Linewidths of the ^{31}P NMR band, measured as the full width at half maximum (FWHM), were reported in Table 1 for conventionality, and inverse linewidths (FWHM^{-1}) were used as the NMR crystallinity metric for comparison to Raman and XRD.

2.3. X-ray powder diffraction experiments

XRD spectra were recorded on an X-ray powder diffractometer using a copper X-ray tube operating at 40 kV and 30 mA (Scintag X1, Thermo Optec Corp, Cupertino, CA). The specimens were scanned at a reflection angle (2θ) of 20° to 37° using a step size of 0.02° with a 2 s/step acquisition time for CAp samples and 10 s/step for biological specimens. The inverse of the FWHM for the *c*-axis reflection band (0 0 2) was used as the measure of crystallinity in the XRD spectra as defined by the Scherrer equation (Eq. (1))

$$L = \frac{K\lambda}{\beta_{cry}\cos\theta} \quad (1)$$

where L is the average crystal domain size, β_{cry} is the FWHM of the reflection band (25.6° 2θ for *c-axis*), K is a constant related to crystal shape (K=0.9), and λ is the wavelength of X-ray radiation (1.54056 Å). Instrument broadening contributes to bandwidth according to a sum of squares shown in Eq. (2)

$$\beta = {\beta_{cry}}^2 + {\beta_{inst}}^2 \quad (2)$$

where β_{inst} is the instrumental broadening term and β is the total broadening measured. Microstrain in the crystal lattice also contributes to broadening, although this is not usually separated from crystallinity in the bone literature [51]. For consistency of measurement, microstrain was not separated from β_{cry} in this study. Instrumental broadening was measured using a LaB_6 standard acquired from NIST (SRM 660b), which was found to be β_{inst}=0.105° 2θ.

2.4. Raman spectroscopy experiments

All Raman experiments were performed using a locally constructed Raman microscope as described elsewhere. [52] The major components of this instrument are a 785 nm diode laser (Invictus, Kaiser Optical Systems, Inc., Ann Arbor, MI), a Nikon E600 epi-fluorescence microscope fitted with a 20*x*/0.75 NA S Fluor objective (Nikon, Inc., Melville, New York), a spectrograph (HoloSpec Kaiser Optical Systems, Inc.) and a deep depletion CCD detector (DU401-BR-DD, Andor Technologies, Belfast, Northern Ireland). Raman data were processed in MATLAB software (The Math Works, Natick, Massachusetts) with corrections for cosmic ray spikes, image curvature, dark current, and variations in the CCD quantum efficiency. Bone spectra were digitally resolved according to protocol reported in Ref. [52]. Four Gaussian–Lorentzian functions were fit in the 900–1010 cm^{-1} region to distinguish the PO_4^{3-} ν_1 band from nearby collagen bands in the powdered bone samples. No band fitting was performed on the CAp spectra as there were no interfering bands. Bandwidths and shifts of the PO_4^{3-} ν_1 symmetric stretch band were reported in a similar fashion to ^{31}P NMR data; that is they were reported as FWHM in Table 1 for conventionality, and inverse bandwidths (FWHM^{-1}) were used as the Raman crystallinity metric. Linear regression analysis was used to compare ^{31}P NMR inverse linewidth to XRD crystallinity and to Raman PO_4^{3-} ν_1 inverse bandwidth, and Raman PO_4^{3-} ν_1 inverse bandwidth to XRD crystallinity for the CAp series. Relationships are reported as r^2-values, linear coefficients and *p*-values.

2.5. Atomic force microscopy

Synthetic CAp mineral powder was suspended in HPLC grade methanol (10 mg/ml). The suspension was sonicated for 30 min in order to reduce aggregation. After sonication, the suspension was immediately diluted to 1 mg/ml and sonicated for another 30 min. Another dilution and 30 min sonication was carried out to reach a final concentration of 0.4 mg/ml. The suspension was then pipetted onto freshly cleaved mica. After resting in air for 3 min, the remaining methanol on the mica surface was wicked off. The dispersed CAp crystals on the mica surface were imaged in air using a PicoPlus 5500 AFM (Agilent, Santa Clara, CA) in tapping mode. Silicon AFM probes were used (VistaProbes T300R, tip radius < 10 nm, force constant 40 N/m, resonance frequency 300 kHz; NanoScience Instruments; Phoenix, AZ). Multiple scan regions ranging from 1.5 μm to 5 μm in size were captured (512 pixels per line). Different scan sizes ranging from 1 μm^2 to 5 μm^2 were chosen to maintain a good resolution for different particle sizes. The height images were background subtracted using plane correction. An open-source software, Gwyddion, was used to mark grains by height thresholding. Particle size of the

Table 1
Composition, crystallinity and spectroscopic broadening of synthetic and biological apatites.

Mineral ID	Chemical analysis (wt%)			Crystallinity (nm)[c]	Raman PO_4^{3-} ν_1		^{31}P NMR	
	CO_3[a]	Ca[b]	P[b]		FWHM (cm^{-1})	Center (cm^{-1})	FWHM (ppm)	δ_{iso} (ppm)
CAp1	0.3 ± 0.1	41.13 ± 0.58	19.13 ± 0.16	86 ± 6	7.3 ± 0.1	961.0 ± 0.1	1.18 ± 0.03	2.91 ± 0.03
CAp2	2.26 ± 0.06	41.27 ± 0.65	18.62 ± 0.18	59 ± 4	9.7 ± 0.2	960.7 ± 0.1	1.58 ± 0.04	2.91 ± 0.04
CAp3	3.5 ± 0.2	41.75 ± 0.55	18.24 ± 0.16	48 ± 5	10.9 ± 0.2	960.8 ± 0.1	1.77 ± 0.06	2.89 ± 0.03
CAp4	5.8 ± 0.1	41.02 ± 0.52	17.51 ± 0.16	35 ± 3	13.3 ± 0.2	960.8 ± 0.1	2.17 ± 0.07	2.90 ± 0.03
CAp5	6.95 ± 0.07	39.03 ± 0.80	17.28 ± 0.16	29.5 ± 0.4	15.7 ± 0.2	959.8 ± 0.1	2.56 ± 0.09	3.10 ± 0.03
CAp6	8.72 ± 0.02	40.87 ± 0.77	16.97 ± 0.16	23 ± 2	16.5 ± 0.3	958.0 ± 0.1	2.6 ± 0.1	3.36 ± 0.04
CAp7	10.3 ± 0.1	40.65 ± 0.64	16.28 ± 0.14	21 ± 2	18.2 ± 0.3	958.3 ± 0.1	3.0 ± 0.1	3.36 ± 0.04
BF bone[d]	7.6 ± 0.4	–	–	27.5 ± 0.8	16.4 ± 0.6	958.0 ± 0.1	2.7 ± 0.1	3.50 ± 0.04
MF bone[d]	8.6 ± 0.2	–	–	23 ± 2	18.6 ± 0.3	960.4 ± 0.4	3.1 ± 0.1	3.57 ± 0.04

[a] Carbonate composition for synthetic powders were measured by FTIR and bone powders were measured by Raman and compared to standards for wt% conversion.
[b] Measured by ICP-OES.
[c] Measured by XRD along *c*-axis (0 0 2).
[d] Powdered bone: BF, bovine femur; MF, murine femur.

longest dimension was measured from the marked grains to generate the size distribution.

3. Results and discussion

3.1. Crystallinity and spectroscopic bandwidths

Powder XRD patterns for synthetic apatites containing different carbonate levels have reflection bands that are the same as in hydroxyapatite [53] but that increase in width as carbonate content increases [54]. Carbonate substitution perturbs the lattice generally causing a lower resolution of all reflection bands in the powders with higher carbonate content. *c-axis* crystallinity, which is a crystal size metric commonly reported in bone literature [55], is inversely proportional to the (0 0 2) reflection bandwidth at 25.8° and has been used in this study (Fig. 1A). Reflection bandwidths in the 31–34° region are highly overlapped for the CAps and entirely unresolvable for the bone powders, Therefore, measures of crystallinity were restricted to the *c-axis* for this study. Crystallinities, calculated from the XRD *c-axis* bandwidth for the synthetic apatites, decreased monotonically from 86 nm to 21 nm (Table 1) with increasing carbonate content (0.3–10.3 wt%). Bone powders had carbonate contents of 7.6 wt% and 8.6 wt% with crystallinities consistent with the trend observed in the synthetic apatites.

The ^{31}P NMR spectra of the studied species (Fig. 1B) have similar line shapes, each consisting of a single featureless, broad peak of 2.9–3.6 ppm (ppm) from 85% H_3PO_4(aq), in accordance with the published ^{31}P NMR data for apatite and bone mineral [44,45]. Although chemical shift anisotropy and heteronuclear ^{1}H–^{31}P dipolar coupling were completely eliminated by the high magic-angle sample spinning and high-power proton decoupling respectively, the structureless shapes of the peaks result from the overlapping/superposition of multiple line shapes corresponding to magnetically non-equivalent phosphorous-containing sites, and from the structural disorder in the chemical environment around the phosphorous nuclei. The FWHM linewidth range for the CAp series is 1.18–3.0 ppm and increases with increasing carbonate content, whereas it varies inversely with *c-axis* crystallinity ($r^2=0.99$, $m=0.0076\pm0.0003$, $b=0.19\pm0.01$, $p_m<0.01$, $p_b<0.01$, Fig. 1D). This change in linewidth is mainly due to the continuous distribution of ^{31}P chemical shifts, which is sensitive to local distortions of each phosphate site. Distortions can stem from chemical structural defects as well as slight differences in the chemical composition of the samples.

Raman spectra of the synthetic CAp powders show a similar trend of increasing widths in the PO_4^{3-} ν_1 mineral band with increasing carbonate content (Fig. 1C) and inverse bandwidths correlate with *c-axis* crystallinity ($r^2=0.99$, $m=0.00124\pm0.00004$, $b=0.030\pm0.002$, $p_m<0.01$, $p_b<0.01$, Fig. S1). Similar relationships have been established previously [26,56]. The inverse bandwidth also correlates well with ^{31}P NMR inverse linewidths ($r^2=0.99$, $m=6.18\pm0.08$, $b=-0.001\pm0.007$, $p_m<0.01$, $p_b=0.89$, Fig. 1E).

For bone specimens, both NMR linewidths and Raman bandwidths predicted crystallinities near those measured based on calibration using the synthetic apatite series. NMR linewidths predicted crystallinities of 24.0 ± 4 nm and 17.7 ± 5 nm, and Raman bandwidths predicted crystallinities of 24.7 ± 4 nm and 19.9 ± 4 nm for BF and MF powders, respectively. These estimates are within standard error of the bovine (27.5 ± 0.8 nm) and murine (23 ± 2 nm) crystallinities measured directly by XRD (Table 1).

3.2. Band shifts and apatite compositional change

^{31}P NMR bands abruptly shifted over a short range of carbonate substitution. The chemical shift remained constant at 2.9 ppm until 5.8% CO_3^{2-}, and then increased, reaching a plateau at 3.36 ppm with 8.72% CO_3^{2-} (Fig. 2A). An abrupt change in chemical shift is indicative of significant structural modification to the whole apatite lattice, consistent with a phase transition. Similar results were observed

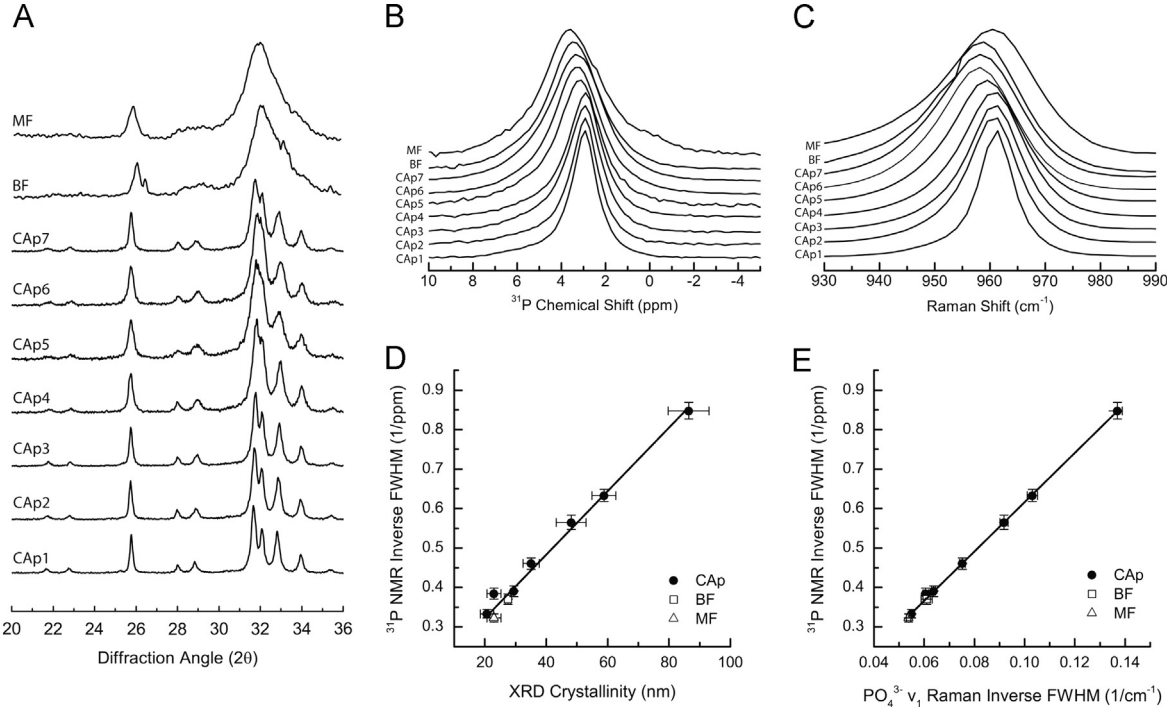

Fig. 1. X-ray diffraction, ^{31}P NMR, and Raman spectral analysis of synthetic carbonated apatites in the 0.3–10.3 wt% range (CAp1–CAp7, ordered from low to high CO_3^{2-} content), bovine femur (BF), and mouse femur (MF) powdered bone samples. (A) XRD patterns normalized to *c*-axis reflection (0 0 2). (B) Normalized ^{31}P NMR spectra and (C) normalized Raman spectra of PO_4^{3-} ν_1. (D) *X*–*Y* plot of ^{31}P NMR inverse FWHM versus XRD crystallinity with x and y error bars representing standard deviation. (E) *X*–*Y* plot of ^{31}P NMR inverse FWHM versus Raman PO_4^{3-} ν_1 inverse FWHM. *X* and *Y* error bars represent standard deviations.

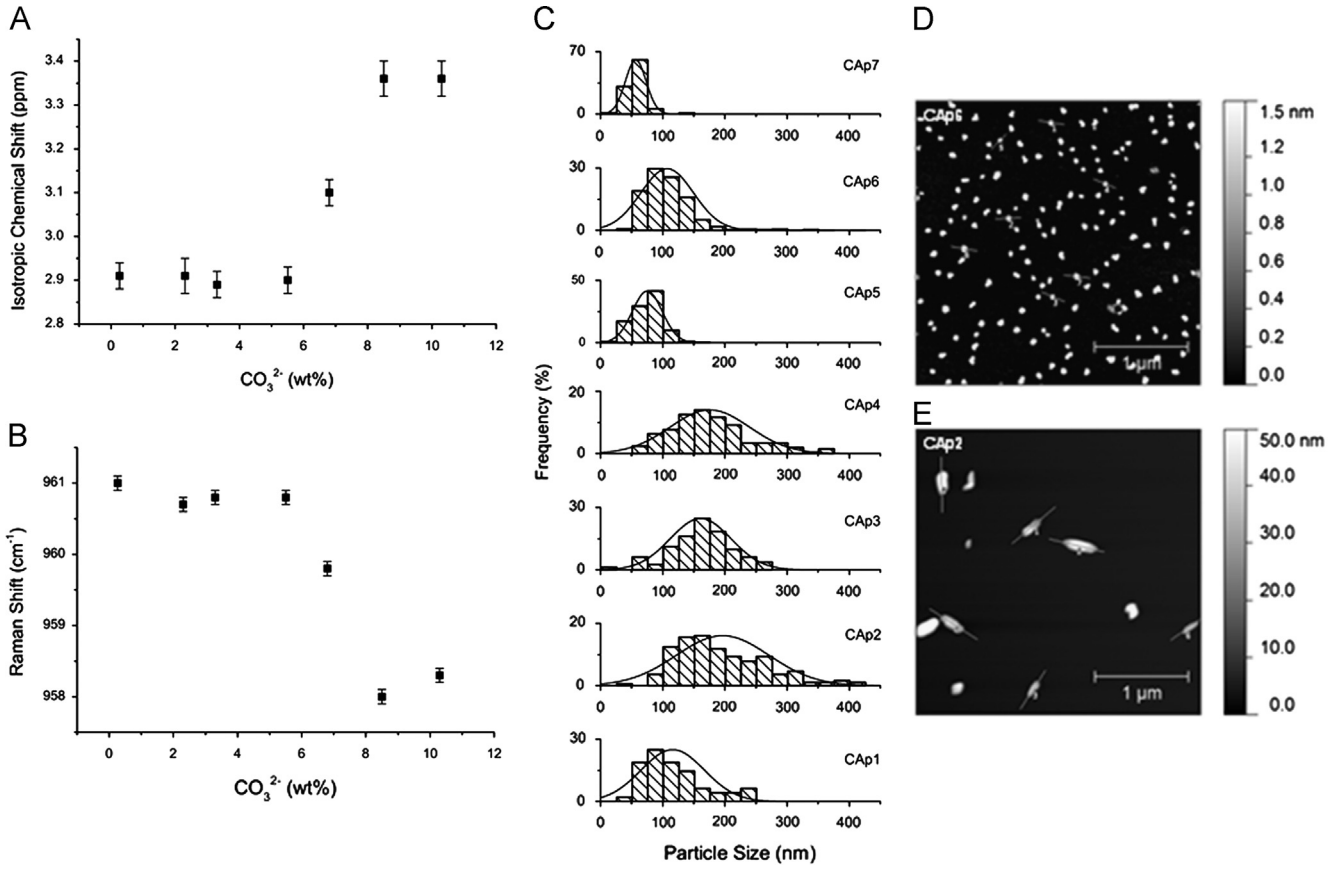

Fig. 2. Characterization of carbonate-induced transition in synthetic carbonated apatites in the 0.3–10.3 wt% range. (A) Measures of ^{31}P NMR chemical shift relative to H_3PO_4, and (B) Raman PO_4^{3-} ν_1 band center versus carbonate content with error bars representing standard deviations. (C) Histograms of carbonated apatite particle size distribution as measured by atomic force microscopy (AFM), with (D) and (E) micrographs of CAp6 (8.72 wt% CO_3^{2-}) and CAp2 (2.26 wt% CO_3^{2-}), respectively.

in the Raman spectra. The PO_4^{3-} ν_1 band center remained constant at 961 cm^{-1} with increasing carbonate until 5.8% CO_3^{2-}, and then shifted to 958 cm^{-1} at 8.72 wt% CO_3^{2-} and higher (Fig. 2B). Shifts in PO_4^{3-} ν_1 have been seen in other biological apatite studies in relation to mineral maturity [57]. The bone apatites in this study did not strictly adhere to the carbonate-induced shift phenomenon, which suggests that more factors may be relevant in bone mineral. Both bone samples had carbonate contents in the transition region of 5.8–8.72 wt% CO_3^{2-}. The bovine sample had a chemical shift of 3.50 ppm which is 0.14 ppm more down field from the high carbonate containing synthetic apatites, although the PO_4^{3-} ν_1 Raman band was consistent with the high carbonate synthetic apatites at 958.0 cm^{-1}. The murine sample also had a chemical shift more down field at 3.57 ppm, but had a PO_4^{3-} ν_1 band centered at 960.4 cm^{-1} similar to low carbonated synthetic apatites. In the bone powders, crystallinities were consistent with synthetic apatites of similar carbonate levels however, other ion substitutions (primarily Na^+, Mg^{2+}, and F^-) in the apatitic mineral, as well as collagen and other mineral-binding proteins, likely have a significant effect on surface properties of the apatite crystals which may be underlying factors to spectroscopic band shifts.

Particle sizing by AFM showed a near-binary distribution of sizes with a shift in size distributions occurring in the 5.8–8.72 wt % CO_3^{2-} region, consistent with spectroscopic band shifts (Fig. 2C). In the low carbonate range (<6.5 wt%, CAp1–CAp4), mean particle sizes were 116–196 nm and varied over a wide range (50–74 nm s.d.). In the high carbonate content range (>6.5 wt%, CAp5–CAp7), the mean particle sizes were 56–107 nm and varied less (16–42 nm s.d.). Furthermore, CAp1 and CAp2 powders, containing the lowest amount of carbonate, formed elongated structures while the rest of the CAp powders formed rounded structures with no clear major axis (CAp6 and CAp2 are pictured in Fig. 1D and E, respectively). Although the trend of decreasing particle size with increasing carbonate is generally consistent with measures of crystallinity, the AFM particle sizes do not decrease incrementally as they appear to do by XRD. It is important to point out that XRD crystallinity is not a measure of particle size but rather crystal domain size. AFM particle size may measure many crystal domain regions (and perhaps, aggregates), and therefore tends to have larger values than XRD crystallinity measures. Additionally, internal strain in the crystal may have a sizeable influence on apparent crystallinity that is dependent on substitution of ions. Because the measure of crystallinity is confounded in this study, the contribution of lattice strain cannot be obtained. Instead, the ionic composition of apatites was obtained, which provides a view of lattice vacancies associated with internal strain.

Calcium and phosphate content was measured in the synthetic apatite series by ICP-OES (Table 1). The phosphate content of the synthetic powders decreased from 19.13 wt% (CAp1) to 16.28 wt% (CAp7) with increasing carbonate substitution ($r^2=0.99$, $m=-0.28\pm0.01$, $b=19.21\pm0.07$, $p_m<0.01$, $p_b<0.01$, Fig. S2). This is consistent with the B-type substitution model. Calcium content did not have a linear relationship with carbonate content, but displayed similar binary characteristics observed in other techniques with low carbonated apatites containing calcium above 41 wt% and high carbonated apatites containing calcium below 41 wt% (Fig. S2). Ca/P molar ratio provides a measure of cationic occupancy relative to substitution. CAp1 had a Ca/P ratio consistent with pure hydroxyapatite containing stoichiometric Ca and P in a 5:3 ratio. Ca/P ratios increased linearly with carbonate content for CAp1–CAp4; however CAp5–CAp7 had

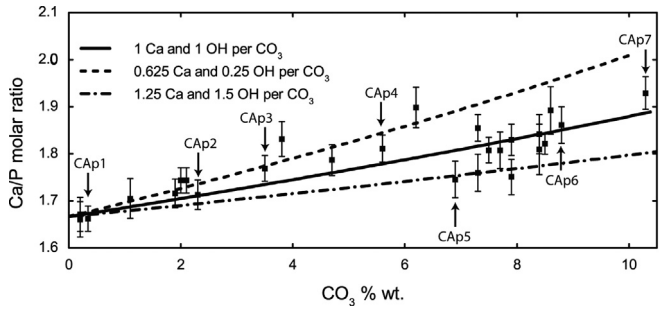

Fig. 3. Plot of compositional analysis, Ca/P molar ratio of 26 B-type carbonated apatites versus CO_3^{2-} wt%. Modeled curves for high-ion loss (1.25 Ca and 1.5 OH per CO_3), medium-ion loss (1 Ca and 1 OH per CO_3) and low-ion loss (0.625 Ca and 0.25 OH per CO_3) are overlayed representing a variety of possible charge-balance mechanisms. *Y*-error bars represent standard deviations. Labeled CAp samples are characterized in Table 1.

significantly lower Ca/P ratios and were not collinear with the lower carbonated apatites (Fig. 3).

In B-type carbonated apatite the CO_3^{2-} substitution for PO_4^{3-} creates a charge imbalance. A wide variety of charge compensation mechanisms have been proposed, which include the concomitant loss of calcium and hydroxide [58,59], the presence of protonated phosphate (HPO_4^{2-}) [60], or the presence of monovalent ions such as Na^+ [59,61]. While all of these are plausible in bone mineral, the synthetic conditions for the CAps (high pH, low sodium) leave the first as the only likely mechanism. Furthermore, calcium and hydroxide loss is evident in our CAps (Fig. S3) and in previous reports on synthetic CAps [54,62]. In particular, hydroxide levels in bone have been shown to be very low by Raman and NMR studies [35,63]. The combined loss of calcium and hydroxide ions as carbonate replaces phosphate in hydroxyapatite can be shown by the chemical formula $Ca_{10-xy}(PO_4)_{6-x}(CO_3)_x(OH)_{2-x(2y-1)}$, where x represents the molar amount of carbonate substitution and y represents the fraction of calcium loss as a proportion of carbonate substitution. Charge neutrality is maintained by an appropriate amount of hydroxide loss per carbonate substituted, expressed as $(2y-1)$. Functions of Ca/P molar ratio versus CO_3^{2-} content were modeled at various values of y representing mechanisms for high-ion loss (1.25 Ca and 1.5 OH per CO_3), medium-ion loss (1 Ca and 1 OH per CO_3), and low-ion loss (0.625 Ca and 0.25 OH per CO_3). These models were compared to Ca/P ratios measured from a larger set of 26 B-type CAp powders synthesized under the same conditions as previously stated including the seven CAp powders characterized by NMR and Raman spectroscopies (Fig. 3). CAps with carbonate content below 6.5 wt% formed apatites by way of a low-ion loss mechanism. CAps with carbonate content above 6.5 wt% formed apatites that varied more in Ca/P ratios which appear to be formed by way of medium-to-high-ion loss mechanisms. Pasteris et al. [59] also found a change in substitution mechanism as the degree of carbonation increased in apatites synthesized in the presence of excess sodium ion. Apatite with one carbonate substituted for phosphate per unit cell has ~6.5 wt% carbonate which seems to be the transition point between charge-balance mechanisms. At levels of carbonate substitution near or above an average of one per unit cell, the defects in apatite are close enough to strongly influence the nearby ions such that greater structural stability is provided by arrangements with higher ion vacancies. This difference in the ionic environment near the phosphate ions between low and high carbonate levels is the likely cause of the spectral shifts in NMR frequency and Raman wavenumbers. It is reasonable to infer that the charge-balance mechanism employed by in vitro crystal formation is sensitive to carbonate concentration in the apatite mineral, with one carbonate per unit cell marking the transition point.

4. Conclusion

We have analyzed the crystallinity of a series of synthetic apatite minerals with various carbonate levels, mature bovine femur, and mature mouse femur. We established linear relationships among XRD crystallinity, ^{31}P NMR inverse linewidth, and Raman inverse bandwidth. Furthermore, we have found that both ^{31}P NMR chemical shift and Raman PO_4^{3-} ν_1 band positions divide synthetic carbonated apatites into two classes: low carbonate/high crystallinity and high carbonate/low crystallinity. Within these classes the spectral band positions show little carbonate-composition dependence. Furthermore, low carbonate containing apatites compensate for B-type substitution by way of a different charge-balancing ion-loss mechanism than high carbonate containing apatites. Transition between classes occurs near 6.5 wt% when one carbonate occupies each unit cell on average. However, charge balancing in bone mineral is necessarily more complex because of exposure to a wider variety of ions, and thus accessibility of additional charge compensation mechanisms, as well as interaction with mineral-binding proteins. From a broader perspective, we have demonstrated that solid-state NMR provides excellent opportunities to probe the crystallinity of synthetic apatites and bone mineral. It is hoped that our study would stimulate both investigation into the implications of a binary response to carbonate substitution in apatites and broad implementation of the various cutting-edge solid-state NMR techniques using higher magnetic fields and advanced pulse sequences to investigate apatitic minerals in bone and other structurally similar mineral systems.

Acknowledgments

The authors acknowledge funding by NIH grants R01 AR052010, RR023597 and R01 AR047969 and CRIF-NSF grant. J.-D.M. acknowledges support through NIH training grant T90 DK070071. The authors thank A. Awonusi and R. Buckland for synthesis of the carbonated apatites.

Appendix A. Supporting information

Supplementary data associated with this article can be found in the online version at http://dx.doi.org/10.1016/j.jssc.2013.08.011.

References

[1] D. Faibish, S.M. Ott, A.L. Boskey, Clin. Orthop. Relat. Res. 443 (2006) 28–38.
[2] D. Felsenberg, S. Boonen, Clin. Ther. 27 (2005) 1–11.
[3] S. Chatterji, J.C. Wall, J.W. Jeffery, Calcified Tissue Int. 33 (1981) 567–574.
[4] R.G. Hanschin, W.B. Stern, Bone (1995) 355S–363S.
[5] A.L. Boskey, E. DiCarlo, E. Paschalis, P. West, R. Mendelsohn, Osteoporos Int. 16 (2005) 2031–2038.
[6] E.P. Paschalis, F. Betts, E. DiCarlo, R. Mendelsohn, A.L. Boskey, Calcified Tissue Int. 61 (1997) 487–492.
[7] R. Mendelsohn, E.P. Paschalis, P.J. Sherman, A.L. Boskey, Appl. Spectro. 54 (2000) 1183–1191.
[8] P.G. Robey, in: J.P. Bilezikian, L.G. Raisz, T.J. Martin (Eds.), Principles of Bone Biology, Academic Press, Burlington, 2008, pp. 335–350.
[9] P.G. Robey, A.L. Boskey, in: C.J. Rosen (Ed.), Primer on the Metabolic Bone Diseases and Disorders of Mineral Metabolism, The American Society for Bone and Mineral Research, Washington DC, 2008.
[10] R.Z. LeGeros, in: P.W. Brown, B. Constantz (Eds.), Hydroxyapatite and Related Materials, CRC Press, Boca Raton, 1994, pp. 3–28.
[11] H.A. Lowenstam, S. Weiner, On Biomineralization, Oxford University Press, Inc., New York, 1989.
[12] C. Abjornson, J.M. Lane, Bone Grafts and Bone Graft Substitutes, in: G.E. Friedlaender, H.J. Mankin, V.M. Goldberg (Eds.), American Academy of Orthopaedic Surgeons, Rosemont, IL, 2006, pp. 9–20.
[13] C.G. Finkemeier, J. Bone Joint Surg. Am. 84 (2002) 454–464.
[14] A. Bigi, S. Panzavolta, K. Rubini, Chem. Mater. 16 (2004) 3740–3745.
[15] S. Kannan, A.F. Lemos, J.M.F. Ferreira, Chem. Mater. 18 (2006) 2181–2186.

[16] M.J. Glimcher, Medical Mineraology and Geochemistry, in: N. Sahai, M.A.A. Schoonen (Eds.), Mineralogical Soc Amer, Chantilly, 2006, pp. VA, 223–282.
[17] H. Furuya, S. Matsunaga, Y. Tamatsu, T. Nakano, M. Yoshinari, Y. Ide, S. Abe, Mater. Trans. 53 (2012) 980–984.
[18] S.J. Eppell, W. Tong, J.L. Katz, L. Kuhn, M.J. Glimcher, J. Orthop. Res. 19 (2001) 1027–1034.
[19] A.A. Baig, J.L. Fox, R.A. Young, Z. Wang, J. Hsu, W.I. Higuchi, A. Chhettry, H. Zhuang, M. Otsuka, Calcified Tissue Int. 64 (1999) 437–449.
[20] N. Pleshko, A. Boskey, R. Mendelsohn, Biophys. J. 60 (1991) 786–793.
[21] D. Farlay, G. Panczer, C. Rey, P.D. Delmas, G. Boivin, J. Bone Miner. Metab. 28 (2010) 433–445.
[22] S. Mangialardo, V. Cottignoli, E. Cavarretta, L. Salvador, P. Postorino, A. Maras, Appl. Spectro. 66 (2012) 1121–1127.
[23] O. Akkus, F. Adar, M.B. Schaffler, Bone 34 (2004) 443–453.
[24] O. Akkus, A. Polyakova-Akkus, F. Adar, M.B. Schaffler, J. Bone Miner. Res. 18 (2003) 1012–1019.
[25] J.S. Yerramshetty, C. Lind, O. Akkus, Bone 39 (2006) 1236–1243.
[26] M. Kazanci, P. Fratzl, K. Klaushofer, E.P. Paschalis, Calcified Tissue Int. 79 (2006) 354–359.
[27] M.J. Turunen, S. Saarakkala, L. Rieppo, H.J. Helminen, J.S. Jurvelin, H. Isaksson, Appl. Spectro. 65 (2011) 595–603.
[28] A.E. Aliev, Biopolymers 77 (2005) 230–245.
[29] H. Saito, M. Yokoi, J. Biochem. 111 (1992) 376–382.
[30] E.E. Wilson, A. Awonusi, M.D. Morris, D.H. Kohn, M.M. Tecklenburg, L.W. Beck, Biophys. J. 90 (2006) 3722–3731.
[31] P. Zhu, J. Xu, N. Sahar, M.D. Morris, D.H. Kohn, A. Ramamoorthy, J. Am. Chem. Soc. 131 (2009) 17064–17065.
[32] J. Xu, P. Zhu, M.D. Morris, A. Ramamoorthy, J. Phys. Chem. B 115 (2011) 9948–9954.
[33] J. Kolmas, M. Szwaja, W. Kolodziejski, J. Pharm. Biomed. Anal. 61 (2012) 136–141.
[34] W.P. Aue, A.H. Roufosse, M.J. Glimcher, R.G. Griffin, Biochemistry 23 (1984) 6110–6114.
[35] G. Cho, Y. Wu, J.L. Ackerman, Science 300 (2003) 1123–1127.
[36] Y. Wu, J.L. Ackerman, H.M. Kim, C. Rey, A. Barroug, M.J. Glimcher, J. Bone Miner. Res. 17 (2002) 472–480.
[37] J. Xu, P. Zhu, Z. Gan, N. Sahar, M. Tecklenburg, M.D. Morris, D.H. Kohn, A. Ramamoorthy, J. Am. Chem. Soc. 132 (2010) 11504–11509.
[38] A. Kaflak-Hachulska, D. Chmielewski, A. Gorecki, A. Slosarczyk, W. Kolodziejski, Solid State Nucl. Magn. Reson. 29 (2006) 345–348.
[39] L.T. Kuhn, M.D. Grynpas, C.C. Rey, Y. Wu, J.L. Ackerman, M.J. Glimcher, Calcified Tissue Int. 83 (2008) 146–154.
[40] K.H. Mroue, N. MacKinnon, J. Xu, P. Zhu, E. McNerny, D.H. Kohn, M.D. Morris, A. Ramamoorthy, J. Phys. Chem. B 116 (2012) 11656–11661.
[41] A. Asano, C. Tanaka, Y. Murata, Polymer 48 (2007) 3809–3816.
[42] L. Zhang, E.W. Hansen, I. Helland, E. Hinrichsed, A.L.J. Roots, Macromolecule 42 (2009) 5189–5195.
[43] H. Tsuji, S. Kamo, F. Horrii, Polymer 51 (2010) 2215–2220.
[44] A. Kaflak-Hachulska, A. Samoson, W. Kolodziejski, Calcified Tissue Int. 73 (2003) 476–486.
[45] W. Kolodziejski, in: J. Klinowski (Ed.), New Techniques in Solid-State NMR, Springer, Berlin/Heidelberg, 2005, pp. 235–270.
[46] J.M. Wallace, B. Erickson, C.M. Les, B.G. Orr, M.M. Banaszak Holl, Bone 46 (2010) 1349–1354.
[47] J.M. Wallace, Q. Chen, M. Fang, B. Erickson, B.G. Orr, M.M. Banaszak Holl, Langmuir 26 (2010) 7349–7354.
[48] G. Penel, G. Leroy, C. Rey, E. Bres, Calcified Tissue Int. 63 (1998) 475–481.
[49] A. Awonusi, M. Morris, M. Tecklenburg, Calcified Tissue Int. 81 (2007) 46–52.
[50] B.M. Fung, A.K. Khitrin, K. Ermolaev, J. Magn. Reson. 142 (2000) 97–101.
[51] V.M. Rusu, C.H. Ng, M. Wilke, B. Tiersch, P. Fratzl, M.G. Peter, Biomaterials 26 (2005) 5414–5426.
[52] J.D. McElderry, M.R. Kole, M.D. Morris, J. Biomed. Opt. 16 (2011) 071407.
[53] M. Markovic, M.S. Tung, B.O. Fowler, J.P. Cline, Certificate of Analysis, Standard Reference Material 2910, Calcium Hydroxyapatite, 1997, National Institute of Standards and Technology, Gaithersburg, MD, 1997.
[54] A. Krajewski, M. Mazzocchi, P.L. Buldini, A. Ravaglioli, A. Tinti, P. Taddei, C. Fagnano, J. Mol. Struct. 744 (2005) 221–228.
[55] S. Markovic, L. Veselinovic, M.J. Lukic, L. Karanovic, I. Bracko, N. Ignjatovic, D. Uskokovic, Biomed. Mater. 6 (2011) 045005.
[56] F.F. de Mul, M.H. Hottenhuis, P. Bouter, J. Greve, J. Arends, J.J. ten Bosch, J. Dent. Res. 65 (1986) 437–440.
[57] N.J. Crane, V. Popescu, M.D. Morris, P. Steenhuis, J.M.A. Ignelzi, Bone 39 (2006) 434–442.
[58] T.I. Ivanova, O.V. Frank-Kamenetskaya, A.B. Kol′tsov, V.L. Ugolkov, J. Solid State Chem. 160 (2001) 340–349.
[59] J.D. Pasteris, C.H. Yoder, M.P. Sternlieb, S. Liu, Mineral. Mag. 76 (2012) 2741–2749.
[60] R. Astala, M.J. Stott, Chem. Mater. 17 (2005) 4125–4133.
[61] S. Peroos, Z.M. Du, N.H. de Leeuw, Biomaterials 27 (2006) 2150–2161.
[62] M. Vignoles, G. Bonel, D.W. Holcomb, R.A. Young, Calcified Tissue Int. 43 (1988) 33–40.
[63] J.D. Pasteris, B. Wopenka, J.J. Freeman, K. Rogers, E. Valsami-Jones, J.A.M. van der Houwen, M.J. Silva, Biomaterials 25 (2004) 229–238.